A Combined Model to Predict GNSS Precipitable Water Vapor Based on Deep Learning

Ming Shangguan , Meng Dang, Yingchun Yue, and Rong Zou

Abstract—The precipitable water vapor (PWV) is a key parameter to reflect atmospheric water vapor, which can be derived by the global navigation satellite system (GNSS) technique with high accuracy and temporal resolution. PWV is an important parameter for weather forecasts and climate research. To develop a highly accurate PWV prediction model, we first combine the wavelet analysis (Wa), long short-term memory (LSTM) neural network, and autoregressive integrated moving average (ARIMA) algorithms as WLA model for the GNSS PWV prediction. Wa, LSTM, and ARIMA in WLA separate the random noise and predict the nonlinear and linear trends in PWV, respectively. Afterward, the WLA model is compared with LSTM, ARIMA, wavelet neural networks, and the multivariable linear regression (MLR) method. The WLA model shows the best result in the five prediction models in terms of the root-mean-square error (RMSE, 0.19–0.82 mm) and mean absolute error (0.01–0.07), which are 55.48% and 55.32% lower than other models, and Nash–Sutcliffe efficiency coefficient (NSE, 76.53%–99.7%) is 9.42% greater than other models. For further analysis, we also study the WLA performance in different months using one-month's data as training length. The result shows that WLA has good effects in predicting PWV in different months and the average NSE of WLA is 95%. In addition, the predicted PWV of the WLA model within 3 h is found to be accurate and reliable (RMSE < 2 mm, relative error < 0.1, NSE $> 60\%$). This study demonstrates the good performance of WLA to predict GNSS PWV.

Index Terms—Combined model, global navigation satellite system (GNSS), neural networks, precipitable water vapor (PWV) prediction.

I. INTRODUCTION

WATER vapor is an important component of the atmosphere and plays an important role in weather formation. Although the content of water vapor in the atmosphere

Ming Shangguan is with the School of Geography and Information Engineering, China University of Geosciences, Wuhan 430074, China, and also with the Hubei Subsurface Multiscale Imaging Key Laboratory, Institute of Geophysics and Geomatics, China University of Geosciences, Wuhan 430074, China (e-mail: shanggm@cug.edu.cn).

Meng Dang and Yingchun Yue are with the School of Geography and Information Engineering, China University of Geosciences, Wuhan 430074, China (e-mail: dangmeng@cug.edu.cn; 767512087@qq.com).

Rong Zou is with the Institute of Geophysics and Geomatics, China University of Geosciences, Wuhan 430074, China (e-mail: zourong@cug.edu.cn).

is very small, it is closely related to climate change [1], [2]. The amount of water vapor is difficult to measure due to strong variability in space and time. Recently, with the development of the satellite technique, GNSS becomes one of the most potent methods for water vapor detection due to its high accuracy and temporal resolution [3], [4]. Many previous studies use GNSS water vapor data as one of the important parameters to forecast short-term precipitation and the warning of extreme weather, such as torrential rains and hurricanes [5], [6], [7], [8], [9], [10]. Therefore, accurate prediction of GNSS water vapor has an important impact on climate research and weather forecast [11].

Much research in recent years has focused on predicting the precipitable water vapor (PWV) which discovered that there is potential for enhancing the accuracy of PWV prediction [12], [13], [14], [15], [16]. One way to improve the accuracy is to adopt a deep neural network that can improve the capability of the model by providing complex nonlinear systems and a higher level of abstraction for the model [17]. The deep neural network has been extensively used in meteorology, hydrology, transportation, and other fields in recent decades [18], [19], [20]. For example, Akbari Asanjan et al. [21], Khaniani et al. [22], and Liu et al. [1] completed precipitable predictions based on the long short-term memory (LSTM), support vector machine (SVM), and artificial neural network, respectively. In terms of atmospheric water vapor prediction, Pozo et al. [12] predicted PWV at ALMA site based on the YSU-Noah configuration in which root-mean-square error (RMSE) is 0.7 mm; Sharifi and Souri [13] used a hybrid LS-HE and LS-SVM model to predict PWV and the bias and standard deviations between the observed and predicted values are about 0.37 mm and 3 mm; Ge [23] and Ge et al. [24] used a wavelet neural network (WNN) to predict PWV, in which the RMSE is 0.2 mm on average; Xie et al. [25] showed that the RMSE of the genetic WNN prediction method used PWV sampled at a frequency of 5 min on August 12 at Wuhan station is 0.124 mm, which is smaller than the BP neural network and WNN; Jain et al. [14] predicted PWV using the least square estimation method, which achieves an RMSE of 0.1 mm for the forecasting internal of 5 min in the future; Huang et al. [26] conducted modeling and PWV prediction based on the improved BP neural network and the average RMSE at HKKP is about 5.142 mm. Turchi et al. [27] applied the autoregressive (AR) technique to predict PWV and RMSE < 1 mm for PWV ≤ 15 mm. An alternative approach to improve the accuracy is using the combined model to predict PWV. For instance, Liu et al. [28] used empirical mode

decomposition combined with a neural network to predict PWV and Wang et al. [15] combined the improved adaptive Kalman filter and radial basis neural network to predict PWV. Compared with traditional models, the prediction accuracy of these combined models is obviously improved.

Previous experiments have established that the deep neural network and its combination models based on one or more stations have good precision in predicting PWV. However, the PWV variability is complex in different regions and seasons including linear and nonlinear terms. These models do not consider separating the random noise and the different components of linear or nonlinear trends in the PWV data, which may have an impact on the results of the forecast.

A combined model of wavelet analysis (Wa), LSTM neural network, and autoregressive integrated moving average (ARIMA) was proposed to predict GNSS PWV, hereinafter referred to as the WLA model. Wa in WLA is used to separate the random noise in PWV data. LSTM and ARIMA, respectively, predict nonlinear and linear parts of the data.

II. DATA AND METHODS

To get GNSS PWV data, observation files of ground GNSS stations need to be processed first. Tropospheric delays are estimated by GNSS data processing and are converted into PWV. After highly accurate GNSS PWV time series are derived, five models are used to predict the PWV. This part briefly introduces PWV derivation methods from ground GNSS stations and algorithms of prediction models.

A. Data Processing

We selected 22 ground GNSS stations at different latitudes in China for experiments. The latitude and longitude of 22 experimental stations are given in Table I. Among them, seven stations (BJFS, CHAN, JFNG, LHAZ, SHAO, URUM, WUH2) are International GNSS Service (IGS) stations; ten stations (AHAQ, AHBB, JSLS, JSLY, JSNT, JSYC, SCLH, SCSN, YNTH, YNYL) are from Crustal Movement Observation Network of China; and five stations in Hong Kong (HKKT, HKOH, HKSL, HKST, HKWS) are from Continuously Operating Reference Stations (CORS).

In advance, GNSS observation files of 22 stations in 2018 are processed into hourly GNSS PWV data by GAMIT [29], [30]. GNSS signals are affected by the atmosphere, which can result in signal delay including ionospheric delay and tropospheric delay. Tropospheric delay mainly refers to the zenith tropospheric delay (ZTD). ZTD can be divided into zenith wet delay (ZWD) and zenith hydrostatic delay (ZHD), and accurate ZHD is necessary for data processing [31]. ZHD is calculated by the following equations [32], [33]:

$$\text{ZHD} = (2.2768 \pm 0.0024) \times (P_s / f(\theta, H)) \tag{1}$$

$$f(\theta, H) = 1 - 0.0026 \times \cos 2\theta + 0.00028 \times H \tag{2}$$

where P_s is the surface pressure of the station (unit: hPa); θ is the latitude of the station; H is the height of the station (unit: km); ZHD is the tropospheric zenith hydrostatic delay (unit: mm).

TABLE I
LATITUDE AND LONGITUDE LIST OF EXPERIMENTAL STATIONS

Stations	Latitude(deg)	Longitude(deg)
AHAQ	30.617	116.991
AHBB	32.905	117.296
BJFS	39.609	115.892
CHAN	43.791	125.443
HKKT	22.445	114.066
HKOH	22.248	114.228
HKSL	22.372	113.928
HKST	22.395	114.184
HKWS	22.434	114.335
JFNG	30.516	114.491
JSLS	31.349	119.419
JSLY	34.722	119.467
JSNT	31.953	120.890
JSYC	33.376	120.019
LHAZ	29.657	91.104
SHAO	31.100	121.200
SCLH	31.390	100.670
SCSN	30.500	105.560
URUM	43.808	87.601
WUH2	30.532	114.357
YNTH	24.118	102.751
YNYL	25.885	99.372

Then ZWD can be obtained by the following equation:

$$\text{ZWD} = \text{ZTD} - \text{ZHD}. \tag{3}$$

Finally, temperature (T), local weighted mean temperature (T_m), the conversion factor (Π), and other parameters are used to obtain the PWV value [34], [35], [36], as shown in the following equations:

$$\text{PWV} = \Pi \times \text{ZWD} = 10^6 / \rho_w R_v \left[(k_3 / T_m) + k_2 \right] \times \text{ZWD} \tag{4}$$

$$T_m = \int (e/T) \, dz / \int \left(e/T^2 \right) dz \tag{5}$$

where ρ_w represents the density of liquid water, and the value is $1 \times 10^6 \text{kg/m}^3$; R_v represents the vapor gas constant and is $461.495 \text{ J} \cdot \text{kg}^{-1} \cdot \text{k}^{-1}$; k_2 and k_3 represent atmospheric physical constants. $k_2 = 22.13 \pm 2.20 \text{ k/hPa}$, $k_3 = (3.739 \pm 0.012) \times 10^5 \text{k}^2/\text{hPa}$; T_m represents the weighted mean temperature of the troposphere, which can be expressed as (5), where T and e are the absolute temperature and water vapor pressure, respectively, in the zenith direction.

B. Prediction Models

We use five prediction models in our studies.

First, LSTM is a specific implementation of recurrent neural network (RNN) and is a powerful method for deep learning of time series data. LSTM introduces a memory cell to solve the problems of gradient disappearance and explosion that occur in RNN invariably. The memory cell contains a memory block, and each memory block has three gate structures, including the forgetting gate, the input gate, and the output gate. These three gate structures can read, write, and reset data [37]. Because the output value of the Sigmoid function is between 0 and 1 and it can

let the information flow through the door or not, the activation functions of the three gates are all S-type functions [38].

Second, ARIMA can identify complex patterns in data and generate predictions, which can be used to analyze and predict univariate time series data. The function of ARIMA is represented by (p, d, q), where p represents the number of autoregression items, d represents the number of nonseasonal differences, and q represents the number of lag prediction errors in the prediction equation. Three steps of establishing ARIMA are identification, estimation, and prediction [39].

Third, a WNN is formed by the combination of wavelet and neural network. Its structure is similar to the radial basis function (RBF) network and retains most of the advantages of the RBF network. Parameters of WNN such as the number of hidden nodes and weights are easier to determine. In addition, WNN has the advantages of fast convergence, high accuracy, and small network scale [40]. WNN adopts a three-layer network structure, including an input layer, hidden layer, and output layer. The number of neurons in the hidden layer is determined by the trying out method, and the activation function is the Morlet wavelet function [41].

Fourth, multivariable linear regression (MLR) refers to the method of establishing a prediction model through correlation analysis of two or more independent variables and one dependent variable. Assuming y is the dependent variable, x_1, x_2,..., x_n are the independent variables, and there is a linear relationship between the independent variables and the dependent variable, the MLR model is as follows:

$$y = b_0 + b_1 x_1 + b_2 x_2 + \cdots + b_n x_n \tag{6}$$

where b_0, b_1,..., b_n are regression coefficients of MLR model.

Fifth, we combined the WLA model with Wa, LSTM, and ARIMA. Wa is an effective tool for studying nonstationary time series than Fourier Transform. Its main advantage is that it can obtain the time, position, and frequency information of the signal at the same time [39]. In the WLA model, Wa is used to separate, denoise, and reconstruct the original data to get the denoised PWV. Furthermore, the change of PWV sequence is not simply linear or nonlinear but a combination of the two. It is found in previous studies that LSTM is beneficial in predicting nonlinear sequences and ARIMA is good at predicting linear sequences, hence LSTM and ARIMA models are used to predict PWV. The nonlinear part of PWV can be largely predicted by LSTM, and the linear part of PWV can be largely predicted by ARIMA. Finally, the standard deviation weighting method is used to obtain the final PWV predicted value. WLA model not only separates the random noise existing in the original PWV sequence but also considers the linear and nonlinear trends. The main process of WLA is shown in Fig. 1.

The WLA prediction is divided into three steps.

Step 1: Wa is carried out to separate the random noise in PWV. The steps of Wa include wavelet decomposition, noise reduction, and reconstruction. "db2" is chosen as the basis function for wavelet decomposition and the number of wavelet decomposition layers is one. Noise reduction is applied to the detail coefficient after wavelet decomposition. Finally, the detail coefficient after noise reduction and the approximate coefficient
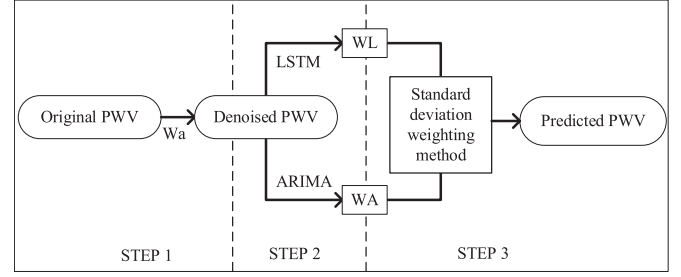

Fig. 1. Main flowchart of the WLA model (WL is the predicted PWV by LSTM, WA is the value predicted by ARIMA).
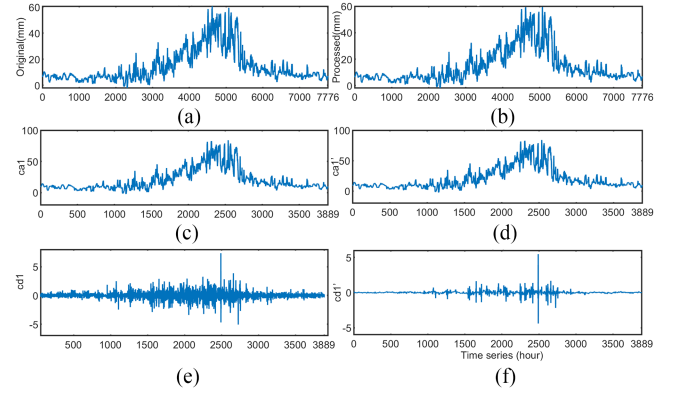

Fig. 2. Original PWV and the sequences decomposed by Wa at CHAN. The horizontal coordinate is the time series of PWV (unit: hour). (a) Sequence of original PWV. (b) First approximation coefficient of wavelet decomposition of original PWV, represented by ca1. (c) Detail coefficients of wavelet decomposition of original PWV represented by cd1. (d) PWV processed by wavelet denoising. (e) Approximation coefficient, represented by ca1', which is the same as ca1. (f) Coefficients after wavelet denoising represented by cd1'.

are reconstructed to obtain the denoised PWV. It showed original PWV and the sequences decomposed by Wa at CHAN in Fig. 2 as an example.

Step 2: The denoised PWV is input into the LSTM and ARIMA model to predict PWV. Enter the training and prediction set of the same time into both models, WL and WA are the predicted data of LSTM and ARIMA, respectively.

Step 3: The standard deviation weighting method, a method to determine the weight coefficient according to the standard deviation of data, is used to assign weights to LSTM and ARIMA. It is obtained by applying the following equations:

$$w_L = \sigma_A^2 / (\sigma_L^2 + \sigma_A^2) \tag{7}$$

$$w_A = 1 - w_L \tag{8}$$

where σ_L^2 and σ_A^2 are the variances of the predicted results of LSTM and ARIMA, w_L and w_A are the weights assigned to LSTM and ARIMA, respectively.

The final predicted value ($\tilde{Y}$) is obtained by the following equation:

$$\tilde{Y} = w_L \times \text{WL} + w_A \times \text{WA}. \tag{9}$$

C. Evaluation Indicators

Evaluation indexes used in this experiment are RMSE, relative error (RE), and Nash–Sutcliffe efficiency (NSE) coefficient.

RMSE is the square root of the ratio of the sum of squares of the deviation between the predicted value and the true value (unit: mm). RE is the ratio of absolute error to the true value (no unit). The calculation formulas of RMSE and RE are shown as follows:

$$\text{RMSE} = \sqrt{(1/N) \sum_{i=1}^{N} (Y_i - f(x_i))^2} \quad (10)$$

$$\text{RE} = (1/N) \sum_{i=1}^{N} |Y_i - f(x_i)/Y_i| \quad (11)$$

where N is the total number, Y is the original value, and $f(x_i)$ is the predicted value.

NSE is generally used to verify the quality of hydrological model simulation results and here is used to verify the quality of PWV prediction models $(-\infty, 1)$. The closer NSE is to 1, the better the quality and reliability of the model. If NSE is much less than 0, the model is not trusted [42]. NSE (expressed as a percentage) is obtained by the following equation:

$$\text{NSE} = \left(1 - \sum_{i=1}^{N} (Y_i - f(x_i))^2 / \sum_{i=1}^{N} (Y_i - \bar{Y})^2\right) \quad (12)$$

where N is the total number, Y is the original value, $f(x_i)$ is the predicted value, and $\bar{Y}$ is the total average value of the original values.

III. EXPERIMENTS AND RESULTS

In this section, we compare the results of WLA with those of the other four models and further analyze the results of the five models in different months. In addition, experiments with different training lengths and different prediction steps based on the WLA model are carried out and the results are analyzed.

A. Model Evaluation

Five models are used to predict PWV in this part, including LSTM, ARIMA, WNN, MLR, and WLA. The prediction results of each model will be compared. These models are trained and evaluated based on one-month's data of PWV. The experiment uses 28 days' data as training data and 3 days' data (72 h) as testing data, and the previous 12 h of PWV are used to predict the next 1-h PWV. Fig. 3 shows the comparison of evaluation indicators at 22 stations of experimental results in January, and Fig. 4 shows the differences in evaluation indicators between WLA and other models. As can be seen from Fig. 3, the error of the WLA model is the smallest at all stations. Conclusions can be drawn from Figs. 3 and 4 that the RMSE of the WLA prediction at each station ranged from 0.19 to 0.48 mm, which was reduced by 6.1%–62.46% compared with LSTM (0.35–1.05 mm), 6.67%–65.86% compared with ARIMA (0.35–1.09 mm), 9.87%–66.63% compared with WNN (0.25–1.05 mm), and 6.45%–62.64% compared with MLR (0.26–1.09 mm). The RE of the WLA prediction
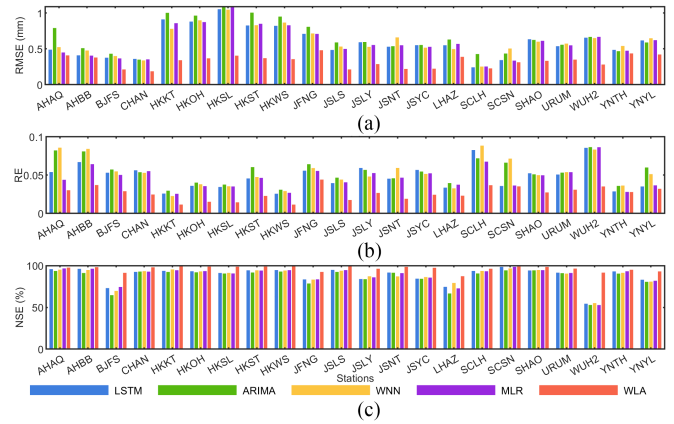

Fig. 3. Evaluation indicators of experimental results at 22 stations of January data. (a), (b), and (c) RMSE, RE, and NSE of different models, where blue represents LSTM, green represents ARIMA, yellow represents WNN, purple represents MLR, and red represents the WLA model.
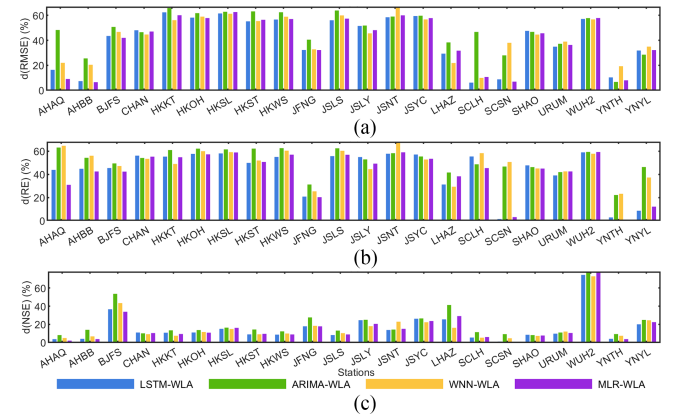

Fig. 4. Variation of evaluation indicators between WLA and other models at 22 stations of January data. (a), (b), and (c) Variation of RMSE, RE, and NSE, where blue is the change between WLA and LSTM, green is the change between WLA and ARIMA, yellow is the change between WLA and WNN, and purple is the change between WLA and MLR.

at each station ranged from 0.01 to 0.04, which was reduced by 1.42%–58.89% compared with LSTM (0.03–0.09), 22.17%–63.08% compared with ARIMA (0.03–0.09), 23.19%–67.74% compared with WNN (0.02–0.09), and 2.41%–59.24% compared with MLR (0.03–0.09). The NSE of the WLA ranged from 87.3% to 99.11%, which was increased by 1.12%–37.24%, 4.06%–37.72%, 3.63%–36.49%, and 3.84%–38.85% compared with LSTM, ARIMA, WNN, and MLR, respectively.

Take BJFS station as an example, Fig. 5 shows the predicted value and error of the PWV prediction by five models at BJFS in January. It is found that the predicted value of PWV from the WLA model is closest to the original value and the error is relatively small compared with other models. Moreover, the peak of PWV value predicted by LSTM, ARIMA, WNN, and MLR in Fig. 5 has a time offset from the original one, while the value predicted by the WLA model has better agreement with the original time series by optimizing lag problems. Therefore, WLA has the best result of the PWV prediction among the five models.
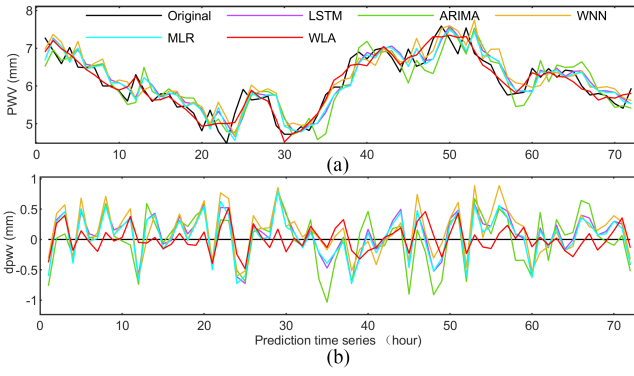
Fig. 5. Value and error of PWV predicted by five models at BJFS in January. The horizontal coordinate is the prediction time series (unit: Hour). (a) Predicted PWV in 72 h by different models. (b) Difference between the predicted PWV and the original PWV. Black line is the original PWV in (a) and the zero line in (b). Predicted PWV of LSTM, ARIMA, WNN, MLR, and WLA are represented by purple, green, yellow, blue, and red lines, respectively.

Fig. 6. Variation of evaluation indicators between WLA and LA at 22 stations of one-year's data in 2018. (a), (b), and (c) Variation of RMSE, RE, and NSE, where blue represents the LA and green represents the WLA model.
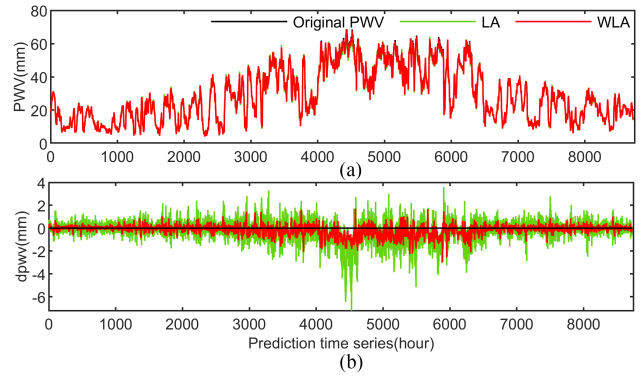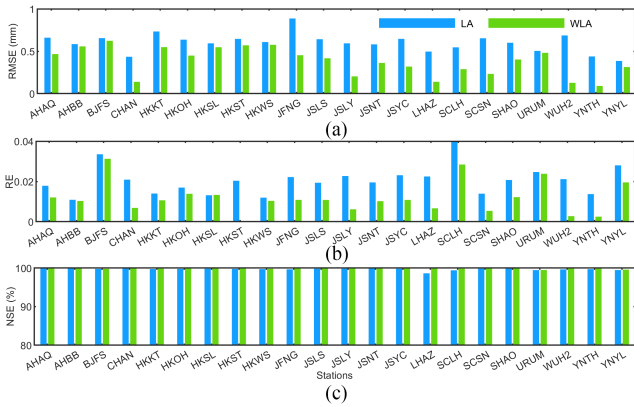

Fig. 7. Value and error of PWV predicted by WLA and LA in 2018 at JFNG. (a) Predicted PWV. (b) Difference between the predicted PWV and the original PWV. Black line is the original PWV in (a) and the zero line in (b). Predicted PWV of LA and WLA are represented by green and red lines, respectively.
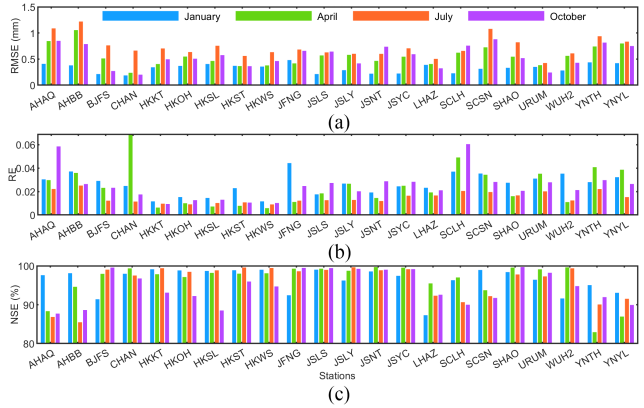

Fig. 8. Evaluation indicators of prediction results of 22 stations in four different months. (a), (b), and (c) RMSE, RE, and NSE, respectively, where blue represents January, green represents April, orange represents July, and purple represents October.

In addition, we conducted experiments on WLA and LA without adding Wa. This experiment used the previous 12 h of PWV to predict the next 1-h PWV in a year. Fig. 6 shows the variation of evaluation indicators between WLA and LA at 22 stations of one-year's data in 2018. It indicates that the RMSE and RE of WLA are smaller than LA and NSE of WLA is higher than that of LA. It can be concluded that Wa can reduce the error in predicting PWV. Fig. 7 is the predicted value and error of the PWV predicted by the WLA and LA at JFNG as an example.

PWV has a significant seasonal change, which is higher in summer and lower in winter. To further check the performance of prediction models in different months, WLA model with the same training lengths is used to predict PWV in each month in 2018. For one month, the first few days are the training period and the last three days (72 h) are the forecast period. Table II lists the range of the evaluation indicators of the different models in different months, from which we can see that the RMSE and RE of WLA are both smaller than those of other models, and NSE is larger than those of other models. Therefore, it can be concluded that the high prediction accuracy of WLA makes it more suitable for PWV prediction.

Fig. 8 shows the evaluation indicators of prediction results of 22 stations based on four different months' PWV. As can be seen from Fig. 8(a), the RMSE in January is relatively small, which is between 0.19 and 0.48 mm; the RMSE in April and October are between 0.24 and 1.06 mm and 0.20 and 0.88 mm, respectively; the RMSE in July is between 0.42 and 1.22 mm, which is relatively large. Fig. 8(b) shows that the RE in four different months is all small. The RE in January, April, July, and October are between 0.01 and 0.04, 0.01 and 0.07, 0.01 and 0.03, and 0.01 and 0.06. And RE of most stations in July is smaller than that of January, April, and October. In Fig. 8(c), we can see that the NSE of each station in four different months is around 95%. It is indicated that WLA has good effects in predicting PWV in different months.

Fig. 8 shows that the RMSE of July is higher than that of other months. It also shows the situation of slightly large RE and low NSE at some stations, such as CHAN and LHAZ. For further analysis, we take CHAN and LHAZ as examples. Compared with other stations, the RMSE in July and RE in April of CHAN is significantly larger and the NSE of LHAZ in January is especially low. PWV predictions at different months

TABLE II
RANGE OF THE EVALUATION INDICATORS OF DIFFERENT MODELS IN DIFFERENT MONTHS

Model	Month	RMSE (mm)	RE	NSE (%)
LSTM	January	0.24-1.05	0.03-0.09	54.36-98.43
ARIMA		0.35-1.09	0.03-0.09	52.89-94.33
WNN		0.25-1.05	0.02-0.09	55.12-96.62
MLR		0.26-1.09	0.03-0.09	50.54-98.50
WLA		0.19-0.48	0.01-0.04	87.3-99.11
LSTM	February	0.39-0.98	0.01-0.09	68.22-98.01
ARIMA		0.42-1.21	0.02-0.09	65.44-97.91
WNN		0.44-1.22	0.02-0.10	60.41-97.43
MLR		0.40-1.17	0.02-0.09	65.80-97.63
WLA		0.33-0.80	0.01-0.09	79.43-98.90
LSTM	March	0.55-1.01	0.02-0.09	68.75-98.13
ARIMA		0.58-0.95	0.02-0.11	66.67-97.04
WNN		0.67-1.06	0.02-0.15	63.43-96.14
MLR		0.52-0.95	0.02-0.12	66.78-96.35
WLA		0.42-0.83	0.02-0.09	75.86-99.15
LSTM	April	0.73-1.42	0.01-0.2	74.79-98.44
ARIMA		0.70-1.49	0.01-0.17	75.48-97.78
WNN		0.75-1.56	0.01-0.20	75.78-98.32
MLR		0.68-1.41	0.01-0.17	75.69-98.46
WLA		0.24-1.06	0.01-0.07	82.93-99.68
LSTM	May	0.47-0.96	0.02-0.10	73.14-98.05
ARIMA		0.48-1.02	0.01-0.09	72.49-97.83
WNN		0.55-1.06	0.02-0.13	73.06-97.92
MLR		0.51-1.02	0.01-0.09	75.25-98.36
WLA		0.36-0.87	0.01-0.06	85.82-99.38
LSTM	June	0.66-1.25	0.01-0.08	73.89-91.24
ARIMA		0.73-1.68	0.01-0.09	73.68-89.75
WNN		0.66-1.32	0.01-0.12	72.13-88.53
MLR		0.62-1.33	0.01-0.08	73.20-89.03
WLA		0.41-0.89	0.01-0.06	81.60-98.96
LSTM	July	0.89-2.27	0.02-0.05	75.73-97.67
ARIMA		1.10-2.19	0.02-0.05	23.51-97.65
WNN		0.92-2.31	0.02-0.05	74.19-97.11
MLR		0.88-2.23	0.02-0.05	76.53-97.61
WLA		0.42-1.22	0.01-0.03	85.48-99.63
LSTM	August	0.57-1.23	0.01-0.07	61.35-95.60
ARIMA		0.57-1.25	0.01-0.07	58.62-95.36
WNN		0.65-1.50	0.01-0.07	61.25-95.60
MLR		0.54-1.21	0.01-0.06	65.12-96.33
WLA		0.35-0.97	0.01-0.05	79.32-98.78
LSTM	September	0.39-1.98	0.01-0.07	66.12-96.37
ARIMA		0.35-2.12	0.01-0.07	63.86-95.81
WNN		0.38-1.82	0.01-0.08	58.42-94.77
MLR		0.35-1.80	0.01-0.07	63.25-95.12
WLA		0.26-1.18	0.01-0.06	79.67-98.63
LSTM	October	0.42-1.51	0.02-0.07	59.77-98.61
ARIMA		0.37-1.94	0.03-0.08	39.46-98.60
WNN		0.40-1.57	0.02-0.07	55.64-98.44
MLR		0.37-1.54	0.02-0.06	62.90-98.70
WLA		0.20-0.88	0.01-0.06	87.71-99.70
LSTM	November	0.46-0.95	0.01-0.09	74.11-98.37

TABLE II
(CONTINUED.)

TABLE II
(CONTINUED.)

ARIMA		0.50-1.06	0.01-0.12	73.27-98.30
WNN		0.57-1.32	0.01-0.08	73.06-97.92
MLR		0.53-1.21	0.01-0.09	72.35-97.86
WLA		0.24-0.73	0.01-0.06	87.71-99.24
LSTM		0.41-1.45	0.02-0.11	71.25-97.80
ARIMA		0.46-1.48	0.02-0.12	71.22-97.68
WNN	December	0.57-1.60	0.02-0.12	68.35-97.64
MLR		0.52-1.48	0.02-0.11	65.21-97.18
WLA		0.23-1.06	0.02-0.10	81.03-98.47
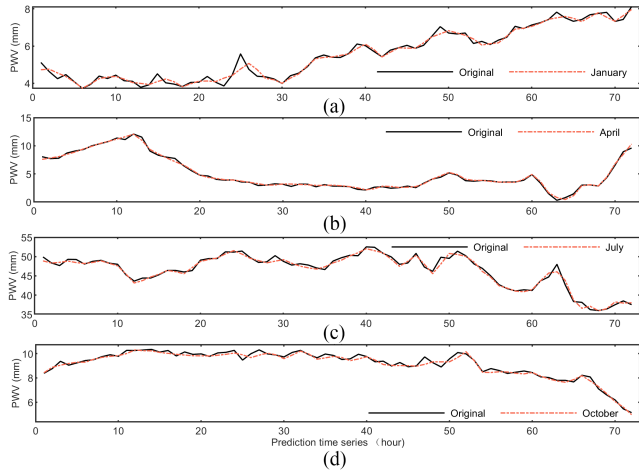
Fig. 9. Original and predicted PWV at CHAN in different months. (a), (b), (c), and (d) PWV of January, April, July, and October, respectively, where the black line represents the original PWV and the red lines represent the predicted PWV.

of CHAN and LHAZ are shown in Figs. 9 and 10. As can be seen from Fig. 9, the large value of PWV in July and the small value of PWV in April at CHAN make the RMSE and RE larger than in other months. What is more, PWV data at CHAN in April fluctuate less than in January, July, and October, which results in the NSE in April being the best. In Fig. 10, we can see that the PWV value of the four different months does not differ much, and therefore, the RMSE and RE do not differ much at LHAZ. The PWV of July is relatively larger and the PWV of January is smaller than other months, so the RMSE in July and RE in January are larger than those of others. On the other hand, the PWV fluctuates greatly in January, so the NSE is smaller than
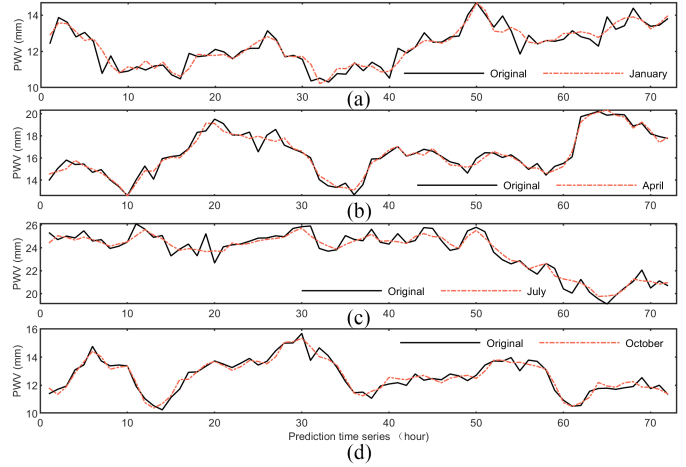

Fig. 10. Original and predicted PWV at LHAZ in different months. (a), (b), (c), and (d) PWV of January, April, July, and October, respectively, where the black line represents the original PWV and the red lines represent the predicted PWV.
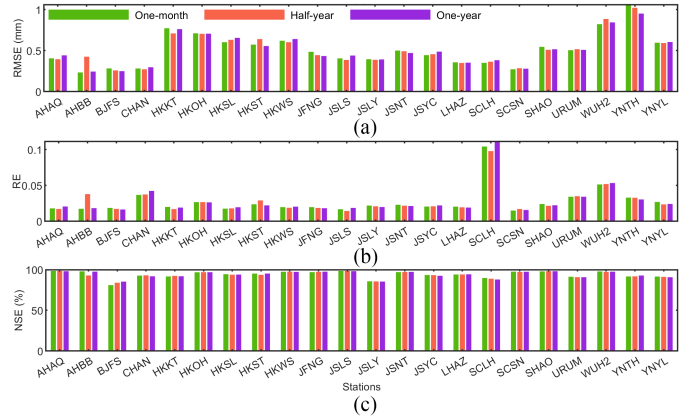

Fig. 11. Evaluation indicators with different training lengths in December. (a), (b), and (c) RMSE, RE, and NSE, respectively, where green represents one-month, red represents half-year, and purple represents one year.

in other months; the fluctuation is small in April, so the NSE is larger than in other months.

In general, the RMSE of PWV prediction in different months are all less than 1.22 mm, the RE in different months are all less than 0.1 and NSE are greater than 75.86%. It indicated that WLA can be applied to the PWV prediction of the different months with different PWV values.

B. WLA Based on Different Training Lengths

WLA model is used to predict PWV with different training lengths in this section. It predicts the last 3 days (72 h) PWV in December with the data of one month, half-year, and one year. Fig. 11 shows the evaluation indicators with different training lengths in December. For predicting the last 3 days (72 h) PWV by one-month's data, the range of RMSE, RE, and NSE is 0.28–1.01 mm, 0.02–0.1, and 83.98%–98.59%, respectively. For predicting the PWV by half-year's data, the range of RMSE, RE, and NSE is 0.26–1.02 mm, 0.01–0.1, 83.98%–98.59%,
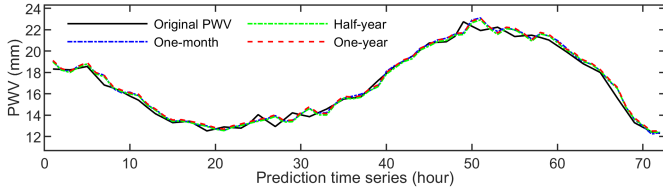
Fig. 12. Predicted PWV of different training lengths in December at AHAQ, where black represents the original PWV, blue represents the predicted PWV by one-month's data, green represents the predicted PWV by half-year's data, and red represents the predicted PWV by one-year's data.
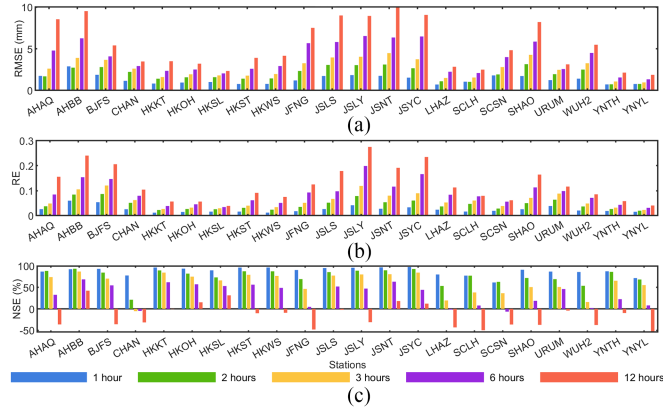

Fig. 13. Evaluation indicators of PWV prediction with different prediction steps in June. (a), (b), and (c) RMSE, RE, and NSE, respectively, where blue represents step 1 h, green represents 2 h, yellow represents 3 h, purple represents 6 h, and red represents 12 h.
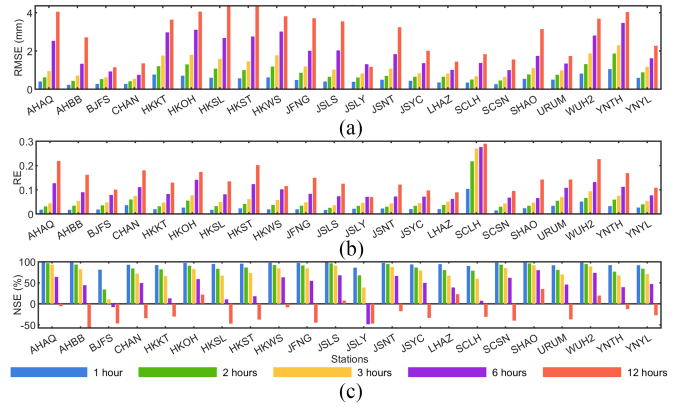

Fig. 14. Evaluation indicators of PWV prediction with different prediction steps in December. (a), (b), and (c) RMSE, RE, and NSE, respectively, where blue represents step 1 h, green represents 2 h, yellow represents 3 h, purple represents 6 h, and red represents 12 h.

TABLE III
AVERAGE VALUES OF THREE INDICATORS WITH DIFFERENT PREDICTION STEPS IN JUNE

Prediction step	RMSE (mm)	RE	NSE (%)
1 h	1.24	0.03	88.19
2 h	2.01	0.04	76.26
3 h	2.69	0.06	59.56
6 h	3.89	0.09	33.56
12 h	5.44	0.12	-16.16

TABLE IV
AVERAGE VALUES OF THREE INDICATORS WITH DIFFERENT PREDICTION STEPS IN DECEMBER

Prediction step	RMSE (mm)	RE	NSE (%)
1 h	0.51	0.03	94.08
2 h	0.84	0.05	84.47
3 h	1.17	0.07	73.06
6 h	1.96	0.1	40.66
12 h	2.86	0.15	-20.49

respectively. For predicting the PWV by one-year's data, the range of RMSE, RE, and NSE is 0.24–0.95 mm, 0.02–0.11, and 85.35%–98.25%, respectively.

We found that the differences in evaluation indicators among one month, half-year, and one year are very small, which indicates that increasing the training length has little effect on the accuracy of PWV prediction. It is observed that the predicted PWV by the data of one month, half-year, and one-year fit the original PWV almost as well in Fig. 12. All results show that PWV predictions of the WLA model can be made by using one month as the length of the training data.

C. WLA Based on Different Prediction Steps

PWV is of vital importance to the study of precipitation in meteorology and space geodesy. Precipitation forecast in meteorology is not simply predicting the next time but time series in the future invariably. Accordingly, this part increases the prediction step from 1 to 2, 3, 6, and 12 h. Two months' data (June and December) of 22 stations are used to predict PWV in this experiment. Evaluation indicators of the results at 22 stations with different prediction steps are shown in Figs. 13 and 14; the average RMSE, RE, and NSE of June and December with different prediction steps are given in Tables III and IV.

It can be observed in Figs. 13 and 14 and Tables III and IV that the RMSE and RE of these 22 stations increase as the prediction step increases gradually. Appreciably, RMSE in June of all stations are less than 3 mm at 1 h (average 1.24 mm),

2 h (average 2.01 mm), 3 h (average 2.69 mm), and increase to 3–5 mm at 6 h (average 3.89 mm) and 12 h (average 5.44 mm); RE of most stations are less than 0.1 at 1 h (average 0.03), 2 h (average 0.04), 3 h (average 0.06), and increase to 0.1–0.2 at 6 h (average 0.09) and 12 h (average 0.12). In December, the RMSE of all stations are less than 2 mm at 1 h (average 0.51 mm), 2 h (average 0.84 mm), 3 h (average 1.17 mm), and increase to 3–5 mm at 6 h (average 1.96 mm) and 12 h (average 2.86 mm);
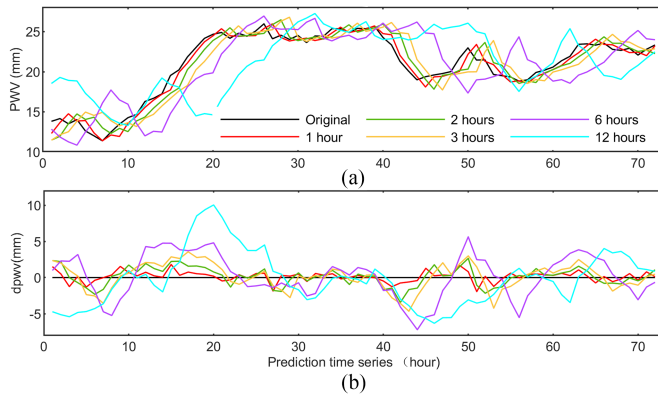
Fig. 15. Results of the HKOH station with different prediction steps in December. (a) Original and predicted PWV. (b) Difference between the predicted and the original PWV of different prediction steps. Red, green, yellow, purple, and blue represent the predicted PWV at the prediction step of 1 h, 2 h, 3 h, 6 h, and 12 h, respectively; black line is the original PWV in (a) and the zero line in (b).

RE of all stations are less than 0.1 at 1 h (average 0.03), 2 h (average 0.05), 3 h (average 0.07), and increase to 0.1–0.2 at 6 h (average 0.1) and 12 h (average 0.15).

In the same way, as the prediction step increases, the NSE of the WLA is getting worse. In June, 14 of 22 stations have NSE at the prediction step in 3 h greater than 60%. NSE in December at the prediction step in 3 h is greater than 60% except for BJFS and JSLY, which illustrated that the WLA model has high reliability of PWV prediction within 3 h. When the prediction step is 6 h, the average NSE in June is 33.56%, and 12 of 22 stations have NSE greater than 40%, and 3 of 22 stations have negative NSE. And the average NSE in December is 40.66%, and 14 of 22 stations have NSE greater than 40%, and 2 of 22 stations have negative NSE. It means that the prediction results for the 6 h prediction step of the WLA model are close to the average level of original PWV. It also means that the overall results for the 6 h prediction step can be used as a reference when the accuracy requirement is not high. When the prediction step is 12 h, negative NSE is present at 16 of 22 stations in June and 17 of 22 stations in December. It has a large error and the results are not accurate, which means WLA model cannot predict PWV with 12 h of prediction steps accurately.

Fig. 15 shows the results of the HKOH station using WLA to predict PWV under different prediction steps and the differences between prediction PWV and original PWV. It shows that the predicted PWV with the prediction step of 1, 2, and 3 h is verging on the original PWV while the error of 6 and 12 h is larger. In conclusion, the WLA model is reliable and accurate in predicting PWV within 3 h and is feasible to predict PWV in 6 h while the accuracy is not high.

IV. Conclusion

WLA model that combined Wa, LSTM, and ARIMA was constructed to predict GNSS PWV. In total, 22 stations in different regions of high, low, and middle latitude in China are used to compare the WLA and other models, including LSTM, ARIMA, WNN, and MLR, and it is observed that WLA has the highest accuracy. The RMSE and RE ranges of the WLA model are 0.19–0.82 mm and 0.01–0.09, which is about 43.2% and 46.58% lower than other models. The NSE, in the range of 87.3%–99.3%, is about 17.62% greater than other models, which means that the WLA model is more stable and credible.

In addition, we analyzed the characteristics of WLA for different months, different training lengths, and different prediction steps. When comparing the results of different months, the average NSE of WLA is around 95%. And we concluded that the RMSE in January, April, and October are less than that in July, while the RE in July is smaller than that of January, April, and October. The results show that the RMSE and RE are closely related to the value of the PWV, and the WLA model has equally good prediction accuracy in different months. For experiments of different training lengths, there is little difference between the result of one month and that of half-year and one year, which can be concluded that one-month training data are enough to predict hourly PWV accurately. Furthermore, we found that the WLA model has high accuracy in predicting PWV with the prediction step of 1–3 h, and the average RMSE is less than 2 mm, RE is less than 0.1, and NSE is around 79.27%. The average RMSE and RE are 2.92 mm and 0.1 when the prediction step is 6 h. And 13 of 22 stations on average have NSE greater than 40%, indicating that the result of 6 h is credible, although the model is not stable enough.

Compared with the predicted results of other models, we found that WLA model has better accuracy in PWV prediction. The Wa in WLA can improve the prediction accuracy by decomposing the random noise from PWV time series. The LSTM and ARIMA models are combined with the help of the standard deviation weighting method. We conducted PWV prediction experiments for different months, different training lengths, and different prediction steps. The results of the PWV prediction experiment in each month show that WLA can be applied to PWV prediction in different months. What is more, we identified that the error of the PWV predicted by WLA model increased with the increase of the prediction step. And WLA can accurately predict the PWV in 3 h.

Overall, we demonstrate that the WLA model has high accuracy in the prediction of PWV and is feasible to predict PWV in the regions we selected and similar regions. It can also predict PWV in different months and different prediction steps, which will be an important promotion for the research meteorology. In future work, we can study how to improve the prediction accuracy and conduct experiments in a larger range by adding data (more stations and a longer period) to confirm the applicability of the model, which can provide powerful data support for further meteorological research.

Acknowledgment

Data Availability: The RINEX data of IGS stations are supplied by the IGS Data Center of Wuhan University (gnsswhu.cn). The RINEX data of CORS stations in Hong Kong are provided by Hong Kong Geodetic Survey Services (geodetic.gov.hk). It can provide the other data to readers by contacting the corresponding author.

REFERENCES

[1] Y. Liu, Q. Zhao, Z. Li, Y. Yao, and X. Li, "GNSS-derived PWV and meteorological data for short-term rainfall forecast based on support vector machine," *Adv. Space Res.*, vol. 70, no. 4, pp. 992–1003, 2022, doi: 10.1016/j.asr.2022.05.057.

[2] Y. Yue and T. Ye, "Predicting precipitable water vapor by using ANN from GPS ZTD data at Antarctic Zhongshan Station," *J. Atmos. Sol. Terr. Phys.*, vol. 191, 2019, Art. no. 105059, doi: 10.1016/j.jastp.2019.105059.

[3] E. Lasota, W. Rohm, G. Guerova, and C.-Y. Liu, "A comparison between ray-traced GFS/WRF/ERA and GNSS slant path delays in tropical cyclone Meranti," *IEEE Trans. Geosci. Remote Sens.*, vol. 58, no. 1, pp. 421–435, Jan. 2020, doi: 10.1109/tgrs.2019.2936785.

[4] Y. Yao, S. Zhang, and J. Kong, "Research progress and prospect of GNSS space environment science," *Acta Geodaetica Cartographica Sinica*, vol. 46, no. 10, pp. 1408–1420, 2017, doi: 10.11947/j.AGCS.2017.20170333.

[5] Q. Zhao, Y. Liu, W. Yao, and Y. Yao, "Hourly rainfall forecast model using supervised learning algorithm," *IEEE Trans. Geosci. Remote Sens.*, vol. 60, 2022, Art. no. 4100509, doi: 10.1109/tgrs.2021.3054582.

[6] Y. G. Ejigu, F. N. Teferle, A. Klos, J. Bogusz, and A. Hunegnaw, "Monitoring and prediction of hurricane tracks using GPS tropospheric products," *GPS Sol.*, vol. 25, no. 2, 2021, Art. no. 76, doi: 10.1007/s10291-021-01104-3.

[7] Q. Zhao, Y. Yao, and W. Yao, "GPS-based PWV for precipitation forecasting and its application to a typhoon event," *J. Atmos. Sol. Terr. Phys.*, vol. 167, pp. 124–133, 2018, doi: 10.1016/j.jastp.2017.11.013.

[8] Q. Zhao, Y. Yao, W. Q. Yao, and Z. Li, "Near-global GPS-derived PWV and its analysis in the El Niño event of 2014–2016," *J. Atmos. Sol. Terr. Phys.*, vol. 179, pp. 69–80, 2018, doi: 10.1016/j.jastp.2018.06.016.

[9] Y. Yao, L. Shan, and Q. Zhao, "Establishing a method of short-term rainfall forecasting based on GNSS-derived PWV and its application," *Sci. Rep.*, vol. 7, no. 1, Sep. 2017, Art. no. 12465, doi: 10.1038/s41598-017-12593-z.

[10] P. Benevides, J. Catalao, and P. M. A. Miranda, "On the inclusion of GPS precipitable water vapour in the nowcasting of rainfall," *Natural Hazards Earth Syst. Sci.*, vol. 15, no. 12, pp. 2605–2616, 2015, doi: 10.5194/nhess-15-2605-2015.

[11] J. Liu et al., "The use of ground-based GPS precipitable water measurements over China to assess radiosonde and ERA-interim moisture trends and errors from 1999 to 2015," *J. Climate*, vol. 30, no. 19, pp. 7643–7667, 2017, doi: 10.1175/jcli-d-16-0591.1.

[12] D. Pozo, L. Illanes, M. Caneo, and M. Cure, "PWV forecast validation at ALMA site," *Revista Mexicana Astronomía y Astrofísica*, vol. 41, pp. 55–58, 2011.

[13] M. A. Sharifi and A. H. Souri, "A hybrid LS-HE and LS-SVM model to predict time series of precipitable water vapor derived from GPS measurements," *Arab. J. Geosci.*, vol. 8, no. 9, pp. 7257–7272, 2014, doi: 10.1007/s12517-014-1716-0.

[14] M. Jain, S. Manandhar, Y. H. Lee, S. Winkler, and S. Dev, "Forecasting precipitable water vapor using LSTMs," presented at the IEEE AP-S Symp. Antennas Propag. USNC-URSI Radio Sci. Meeting, 2020.

[15] J. Wang, J. Huang, K. Xi, and H. Zhu, "Improved prediction model of precipitatable water vapor using adaptive Kalman filter," *Sci. Surv. Mapping*, vol. 42, no. 12, pp. 127–133, 2017, doi: 10.16251/j.cnki.1009-2307.2017.12.022.

[16] W. Suparta and K. M. Alhasa, "A comparison of ANFIS and MLP models for the prediction of precipitable water vapor," presented at the IEEE Int. Conf. Space Sci. Commun., Melaka, Malaysia, 2013.

[17] D. Li and Y. Dong, "Deep learning: Methods and applications," *Found. Trends Signal Process.*, vol. 7, no. 3/4, pp. 197–387, 2014, doi: 10.1561/2000000039.

[18] R. Fu, Z. Zhang, and L. Li, "Using LSTM and GRU neural network methods for traffic flow prediction," presented at the 31st Youth Acad. Annu. Conf. Chin. Assoc. Automat., 2016.

[19] B. Huang et al., "Clock bias prediction algorithm for navigation satellites based on a supervised learning long short-term memory neural network," *GPS Sol.*, vol. 25, no. 2, pp. 1–16, 2021, doi: 10.1007/s10291-021-01115-0.

[20] X. Qing and Y. Niu, "Hourly day-ahead solar irradiance prediction using weather forecasts by LSTM," *Energy*, vol. 148, pp. 461–468, 2018, doi: 10.1016/j.energy.2018.01.177.

[21] A. Akbari Asanjan, T. Yang, K. Hsu, S. Sorooshian, J. Lin, and Q. Peng, "Short-term precipitation forecast based on the PERSIANN system and LSTM recurrent neural networks," *J. Geophys. Res., Atmos.*, vol. 123, no. 22, pp. 12543–12563, 2018, doi: 10.1029/2018jd028375.

[22] A. S. Khaniani, H. Motieyan, and A. Mohammadi, "Rainfall forecast based on GPS PWV together with meteorological parameters using neural network models," *J. Atmos. Sol.-Terr. Phys.*, vol. 214, 2021, Art. no. 105533, doi: 10.1016/j.jastp.2020.105533.

[23] Y. Ge, "Water vapor forecast method research based on wavelet neural network," M.S. thesis, Fac. Geosci. Environ. Eng., Southwest Jiaotong Univ., Chengdu, China, 2014.

[24] Y. Ge, Y. Xiong, Z. Chen, H. Chen, and J. Long, "Prediction method of GPS precipitation based on wavelet neural network," *Sci. Surv. Mapping*, vol. 40, no. 9, pp. 28–32, 2015, doi: 10.16251/j.cnki.1009-2307.2015.09.006.

[25] S. Xie, Y. Su, X. Wang, F. Yang, C. Liang, and Y. Xing, "Prediction of GPS precipitable water based on generatic wavelet neural network," *China Sci. Paper*, vol. 13, no. 9, pp. 1041–1044, 2018.

[26] Y. Huang, G. Wei, and R. Ren, "Improved BP neural network model for prediction of atmospheric precipitable water vapor," *J. Navigation Positioning*, vol. 8, no. 4, pp. 63–67, 2020, doi: 10.16547/j.cnki.10-1096.20200411.

[27] A. Turchi, E. Masciadri, P. Pathak, and M. Kasper, "High accuracy short-term PWV operational forecast at the VLT and perspectives for sky background forecast," *Monthly Notices Roy. Astron. Soc.*, vol. 197, no. 4, pp. 4910–4920, 2020.

[28] Y. Liu, J. Yang, and Y. Wang, "Prediction of GPS water vapor based on EMD and ANN," *Sci. Surv. Mapping*, vol. 38, no. 5, pp. 91–93, 2013, doi: 10.16251/j.cnki.1009-2307.2013.05.048.

[29] T. A. Herring, R. W. King, and S. C. McClusky, "Introduction to GAMIT/GLOBK," Dept. Earth, Atmos., Planetary Sci., Massachusetts Inst. Technol., Cambridge, MA, USA, 2018.

[30] R. Zou, C. Chen, Y. Li, and S. Zhang, *GNSS High Precision Data Precessing-GAMIT/GLOBK Primer*. Beijing, China: China Univ. Geosci., 2019.

[31] W. Zhang, Y. Lou, J. Huang, and W. Liu, "A refined regional empirical pressure and temperature model over China," *Adv. Space Res.*, vol. 62, no. 5, pp. 1065–1074, 2018, doi: 10.1016/j.asr.2018.06.021.

[32] J. H. Saastamoinen, "Atmospheric correction for the troposphere and stratosphere in radio ranging satellites," *Use Artif. Satell. Geodesy*, vol. 15, pp. 247–251, 1972.

[33] H. Li et al., "Detecting heavy rainfall using anomaly-based percentile thresholds of predictors derived from GNSS-PWV," *Atmos. Res.*, vol. 265, 2022, Art. no. 105912, doi: 10.1016/j.atmosres.2021.105912.

[34] M. Bevis, S. Businger, T. A. Herring, C. Rocken, R. A. Anthes, and R. H. Ware, "GPS meteorology: Remote sensing of atmospheric water vapor using the global positioning system," *J. Geophys. Res.*, vol. 97, no. D14, pp. 15787–15801, 1992, doi: 10.1029/92jd01517.

[35] M. Bevis et al., "GPS meteorology: Mapping zenith wet delays onto precipitable water," *J. Appl. Meteorol.*, vol. 33, no. 3, pp. 379–386, 1994.

[36] S. Manandhar, S. Dev, Y. H. Lee, Y. S. Meng, and S. Winkler, "A data-driven approach to detect precipitation from meteorological sensor data," presented at the IGARSS IEEE Int. Geosci. Remote Sens. Symp., Valencia, Spain, 2018.

[37] P. Li, M. Abdel-Aty, and J. Yuan, "Real-time crash risk prediction on arterials based on LSTM-CNN," *Accident Anal. Prev.*, vol. 135, Feb. 2020, Art. no. 105371, doi: 10.1016/j.aap.2019.105371.

[38] H. Wan, S. Guo, K. Yin, X. Liang, and Y. Lin, "CTS-LSTM: LSTM-based neural networks for correlated time series prediction," *Knowl.-Based Syst.*, vol. 191, 2020, Art. no. 105239, doi: 10.1016/j.knosys.2019.105239.

[39] J. Adamowski and H. F. Chan, "A wavelet neural network conjunction model for groundwater level forecasting," *J. Hydrol.*, vol. 407, no. 1/4, pp. 28–40, 2011, doi: 10.1016/j.jhydrol.2011.06.013.

[40] S. Yilmaz and Y. Oysal, "Fuzzy wavelet neural network models for prediction and identification of dynamical systems," *IEEE Trans. Neural Netw.*, vol. 21, no. 10, pp. 1599–1609, Oct. 2010, doi: 10.1109/TNN.2010.2066285.

[41] A. K. Alexandridis and A. D. Zapranis, "Wavelet neural networks: A practical guide," *Neural Netw.*, vol. 42, pp. 1–27, Jun. 2013, doi: 10.1016/j.neunet.2013.01.008.

[42] X. Xu, H. Fan, and G. Li, "Application and correction of the SCS-CN method in runoff estimation of several land use patterns in northeast semi-arid region," *J. Soil Water Conservation*, vol. 33, no. 4, pp. 52–57, 2019, doi: 10.13870/j.cnki.stbcxb.2019.04.008.
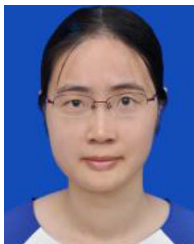
Ming Shangguan received the Ph.D. degree in geodesy and geographic information science from TU Berlin, Berlin, Germany, in 2014.

She was a Researcher with GEOMAR, Kiel, Germany. From 2016 to 2020, she was a Lecturer with Southeast University, Nanjing, China. She is an Associate Professor with the School of Geography and Information, China University of Geosciences, Wuhan, China. Her research interests include GNSS meteorology, atmospheric sounding, and remote sensing.

Yingchun Yue received the Ph.D. degree in geodesy from Wuhan University, Wuhan, China, in 2008.

She was a Post-doc with the China University of Geosciences, Wuhan, China, in 2011. She is an Associate Professor with the School of Geography and Information, China University of Geosciences. Her research interests include GNSS technology application, data processing, and GNSS meteorology in Geodesy.

Meng Dang received the bachelor's degree in 2020 from the China University of Geosciences, Wuhan, China, where she is currently working toward the postgraduate degree.

Her research focuses on GNSS meteorology and its applications.

Rong Zou received the Ph.D. degree in geodesy from Wuhan University, Wuhan, China, in 2010.

She is an Associate Professor with the Institute of Geophysics and Geomatics, China University of Geosciences, Wuhan. Her research interests include geodetic crustal deformation analysis, Earth reference frame, and GNSS data processing.